Importance of Hydrogen Migration in Catalytic Ammonia Synthesis over Yttrium-doped Barium Zirconate Supported Ruthenium Nanoparticles: Visualization of Proton Trap Sites

Christopher Foo[1,2†], Joshua Fellowes[1†], Huihuang Fang[1], Alexander Large,[2] Simson Wu,[1] Georg Held,[2] Elizabeth Raine[1], Ping-Luen Ho[1], Chiu Tang[2], and Shik Chi Edman Tsang[1]*

[†]Authors contributed equally to the work.as co-first authors.

[*]Corresponding author email: edman.tsang@chem.ox.ac.uk

[1]Wolfson Catalysis Centre, Department of Chemistry University of Oxford, Oxford, OX1 3QR, UK
[2]Diamond Light Source, Didcot, OX11 0DE, UK

Supporting Information

Figures and Tables

TEM

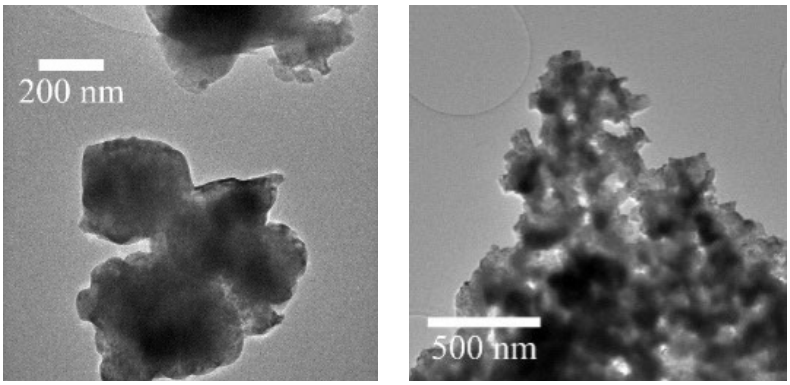

Figure S1. TEM micrographs of the supports (L) Ru-BZEr20, and (R) Ru-BZY20.

X-ray Diffraction

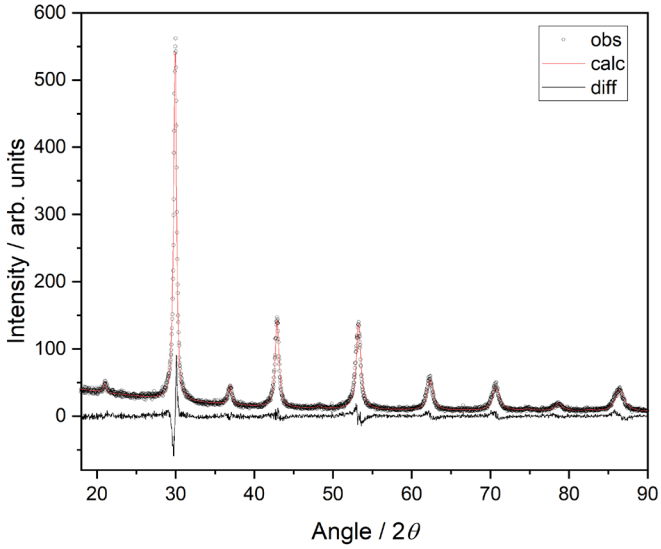

Figure S2. Pawley fitting of pristine BZY20 as an example of a typical fitting (R_{wp} = 11.3).

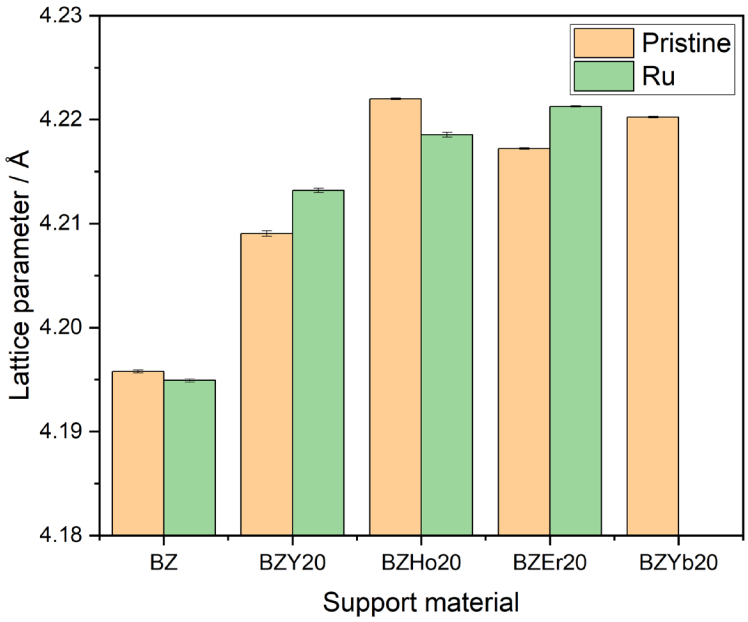

Figure S3. Lattice parameters yielded by Pawley refinement of laboratory-source XRD patterns of the pristine and ruthenium-loaded support materials. Standard deviation expressed as error bars.

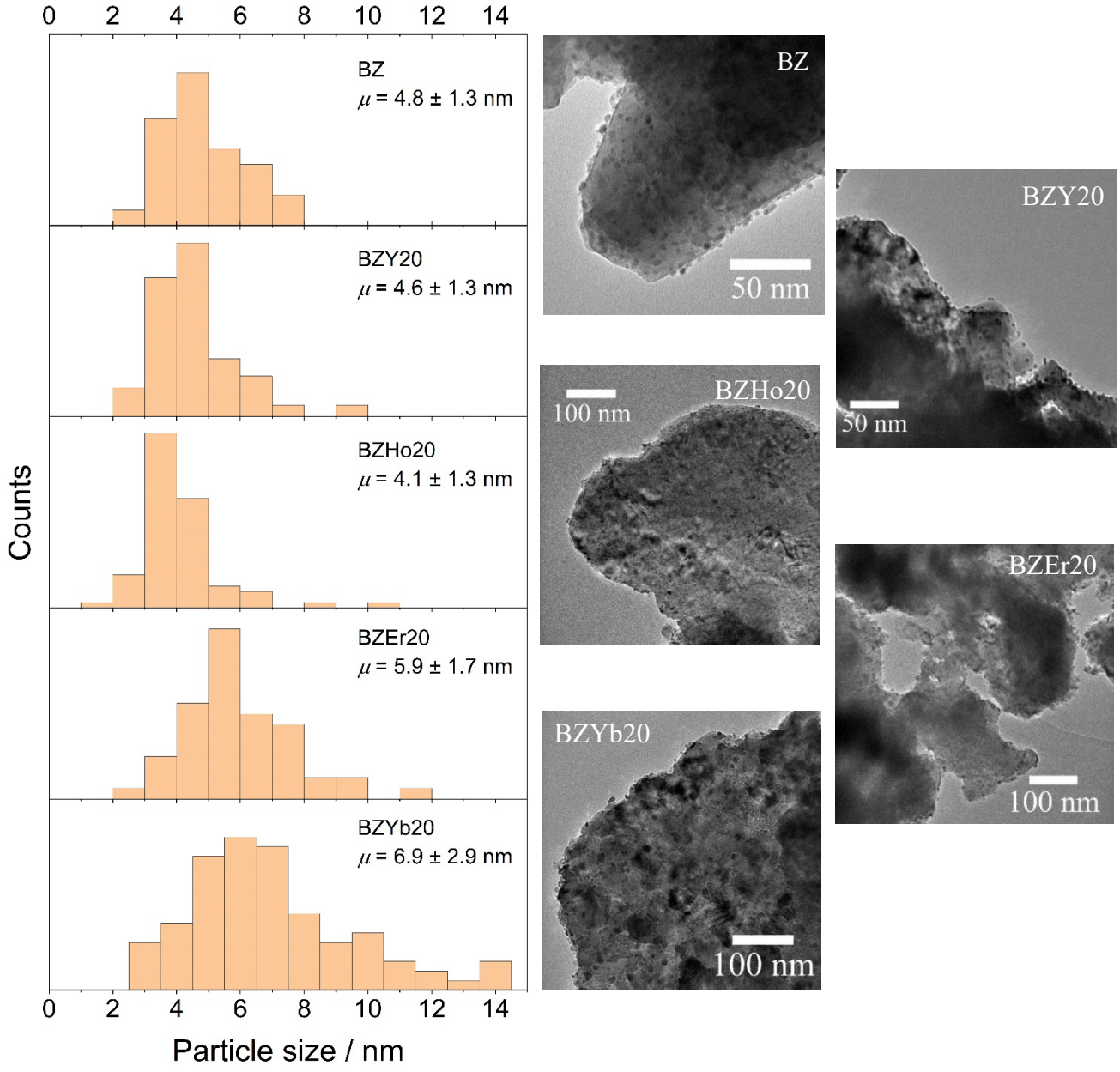

Figure S4. Histograms of ruthenium particle size measurements taken from 50 measurements across multiple micrographs for each sample.

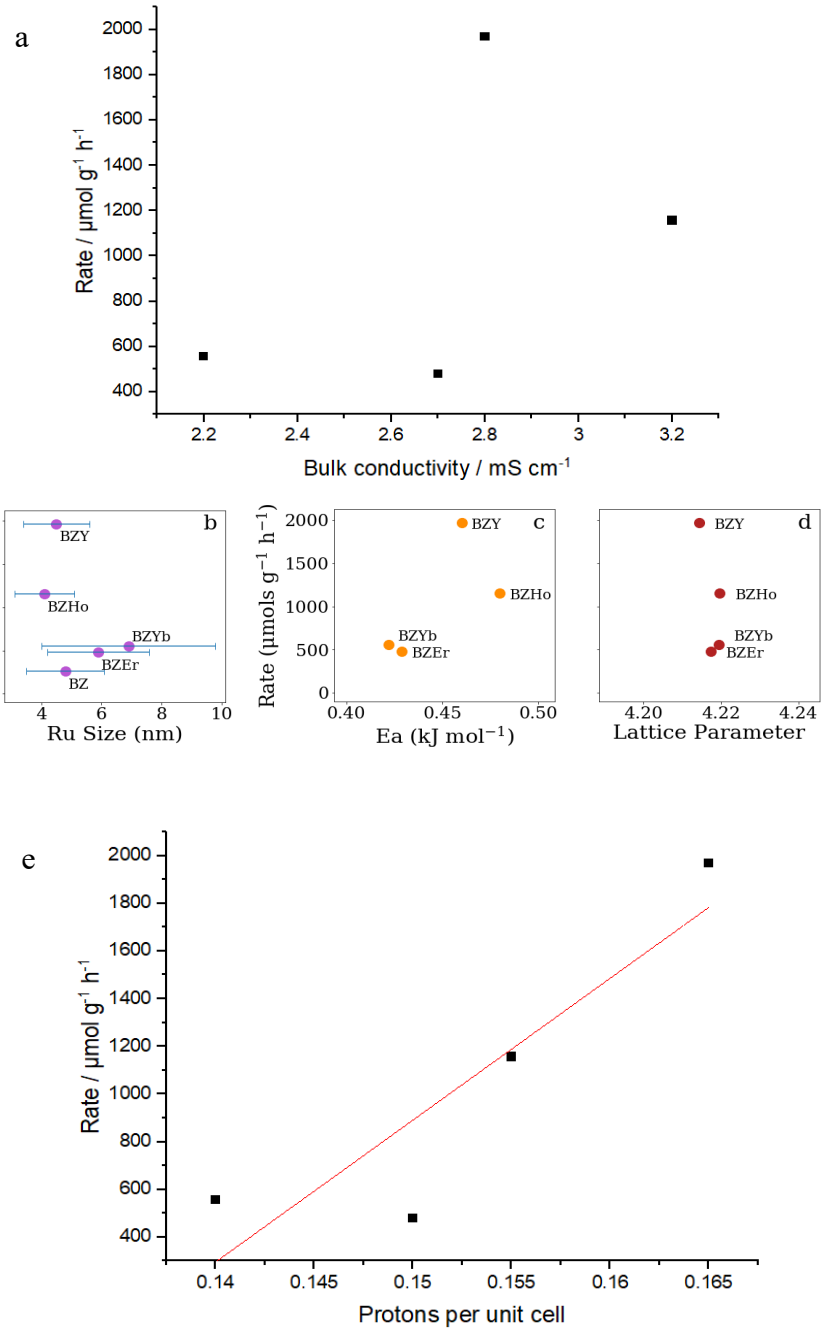

Figure S5. The rates of ammonia synthesis of the four rare-earth-doped BZ samples have no direct correlation with (a) bulk proton conductivity, (b) ruthenium nanoparticle size, (c) proton transport activation energy, (d) lattice parameter. However, there appears to be better correlation with their proton concentration. Non-rate data in (a), (c), and (e) from ref. [1].

Proton conductivity can be in functions of many factors such as sample crystallinity, grain boundaries, and more importantly oxygen vacancies and trapped sites etc. As seen from Fig. S5 that there is a good correlation of rate of ammonia production to their proton concentration per unit cell where Y shows the highest value.

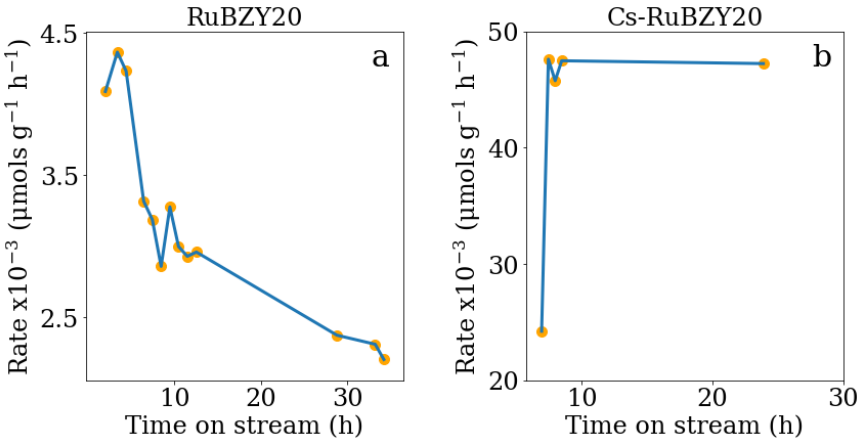

Figure S6. Comparison of (a) RuBZY20 over 34 hours, and (b) Cs-RuBZY20 over 24 hours.

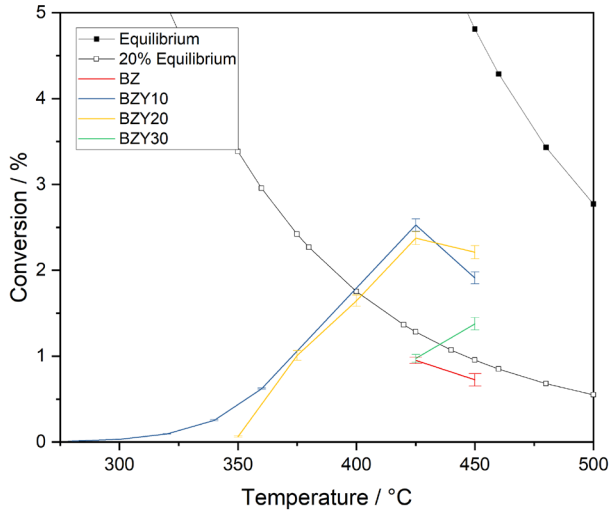

Figure S7. Conversion of feedstock against temperature. Error bars represent standard deviation from at least three rate measurements. Conversion at thermal equilibrium and 20% equlibrium calculated using FactSage software. All experiments carried out with 0.1 g catalyst, 3:1 H_2:N_2, GHSV = 12,400 h^{-1}.

The rates of reaction observed at or beyond 450°C are considered to be limited by back-reaction. It is important to acknowledge that these measurements are still valid observations. It is true that unexpectedly low hydrogen-orders at temperatures approaching equilibrium could be attributed to 'equilibrium-limiting hydrogen-poisoning'; however, only high orders are observed. So, it is acknowledged

that at high temperatures the observed rate of reaction will be being significantly repressed by backward reaction, resulting in a minimum activity that is some fraction of the non-equilibrium limited activity.

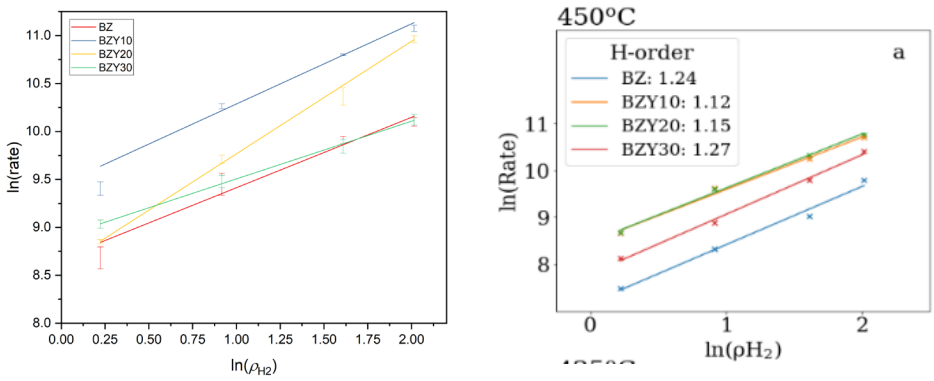

Figure S8. Kinetic analysis of Cs-RuBZY catalysts at (a) 425°C and (b) 450°C.

Comparison to literature performance

Catalyst	Ru wt. %	Temperature / °C	WHSV /mL h^{-1} g^{-1}	Rate /µmol g^{-1} h^{-1}	Rate /mol mol_{Ru}^{-1} h^{-1}	Reference
Cs-Ru/BZY10	***10***	***360***	***120,000***	***14,100***	***14.2***	***This work***
Cs-Ru/BZY20	***10***	***375***	***120,000***	***22,900***	***23.1***	***This work***
Cs-Ru/BZY20	***10***	***400***	***120,000***	***37,400***	***37.8***	***This work***
Ru/C12A7:e^-	1.2	400	18,000	8200	69.1	Kitano et al. 2012
Ru-Ba/AC	9.1	400	18,000	8300	9.2	Kitano et al. 2012
Ru-Cs/MgO	6.0	400	18,000	12,100	20.4	Kitano et al. 2012
Ru/$BaZrO_3$[(a)]	4	375	(10,000 h^{-1})	10,200	25.8	Wang et al. 2013
Ru/$BaZrO_3$[(a)]	4	400	(10,000 h^{-1})	15,300	38.7	Wang et al. 2013
Ru/Pr_2O_3	5	400	18,000	19,000	38.4	Sato et al. 2016
Co-LiH	-	350	60,000	11,500	-	Wang et al. 2017
Fe-LiH	-	350	60,000	10,800	-	Wang et al. 2017
Ru/BZY10	2	400	36,000	4,000	20.2	Shimoda et al. 2017
Ru/$La_{0.5}Ce_{0.5}O_{1.75}$[(b)]	5	400	72,000	65,000	131.4	Ogura et al. 2018
Ru/$La_{0.5}Ce_{0.5}O_{1.75}$[(b)]	5	350	72,000	32,000	64.7	Ogura et al. 2018
Ru/Ba-$Ca(NH_2)_2$	10	360	36,000	60,000	60.6	Kitano et al. 2018
Ru/CeO_2	10	400	60,000	18,000	18.2	Lin et al. 2018
Cs−Ru/MgO(111)	3.7	400	72,000	34,300	93.7	Wu et al. 2020

Table S1. Test conditions and ammonia synthesis rates of literature, and investigated catalysts. Literature data taken from references [2–10] All literature rates are from tests recorded at 3:1 H_2:N_2 and at 1.0 MPa, except (a) and (b) for which 3.0 MPa and 0.9 MPa were used, respectively. WHSV could not be determined for the Ru/$BaZrO_3$ catalyst, so the reported GHSV is given instead.[4]

Further testing

The low temperature catalysis of the most active catalyst Cs-RuBZY10 was tested. It is well-researched that the rate determining step of the HB process is the dissociative adsorption of dinitrogen, and would be expected to be verified by an activation energy ~100 kJ mol^{-1}.[11,12] However, between 280°C and 360°C, the reaction is shown to have an activation energy of 42 kJ mol^{-1} (Figure S7). This value is very low and is more similar to diffusion activated reactions. The value fully agrees with the activation energy found by thermal desorption spectroscopy for the desorption of hydrogen from a loosely bound state that is associated with high overage of hydrogen (42 kJ mol^{-1})[13]. It is proposed that the electron donation from the hydrogen spill-over effect reduces the activation energy for the dissociation of dinitrogen so much that the rate-determining step becomes the removal of poisonous hydrogen from the ruthenium surface. The value is also similar to DFT calculations of activation energy for the dinitrogen dissociation (35 kJ mol^{-1})[14]. This unexpectedly low value can again be explained by reduced activation energy due to hydrogen spill-over. An even lower activation energy analysis was found for Cs-RuBZY20 at high temperatures.

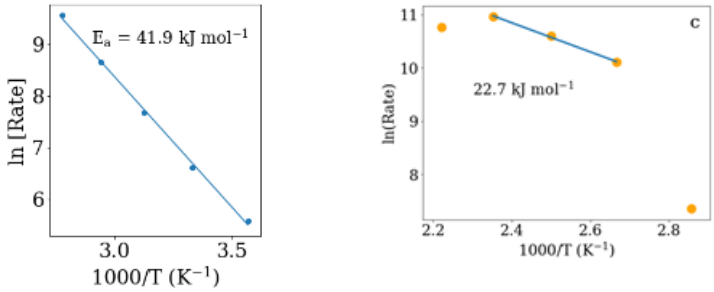

Figure S9. Arrhenius plot from data recorded using Cs-RuBZY10 catalyst (left) and Cs-RuBZY20 catalyst (right) at p_{H2} = 7.5 bar, p_{N2} = 2.5 bar, 10 bar total pressure, 200 mL min^{-1} flow.

As shown in the main manuscript, at the optimal temperature of 425°C, the highest average values of x_{H2} were yielded by BZY20, as well as interestingly not changing at 450°C. Both of these behaviours have been attributed to increased spill-over resulting in reduce hydrogen poisoning and increased strength of

binding. The catalyst was tested at additional temperatures down to 350°C. The data collected using 425°C and 450°C has been discussed in the main manuscript. For the 50°C below 425°C, the peak rate decreases steadily and x_{H2} values approach 0. This is in agreement with greater poisoning at lower temperatures[12]. In this range, an activation energy can be extracted to be 22.7 kJ mol^{-1} (p_{H2} = 7.5 bar).

RuBZ

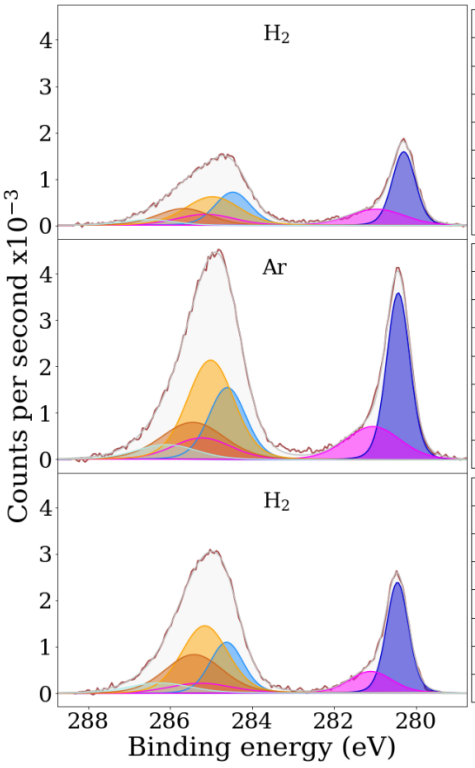

Name	Position	FWHM	Raw Area	%At Conc
$Ru3d_{5/2}$	280.3	0.67	1,181	4.5
$Ru3d_{3/2}$	284.47	1.03	815	3.1
$Ru3d_{5/2(sat)}$	280.96	1.61	622	2.4
$Ru3d_{3/2(sat)}$	285.13	1.65	429	1.6
C-C, C-H	284.96	1.57	1,070	51.0
C-OH	285.67	1.51	596	28.4
C=O	286.51	1.41	188	9.0

Name	Position	FWHM	Raw Area	%At Conc
nan	280.43	0.67	2,666	3.6
$Ru3d_{3/2}$	284.6	1.07	1,839	2.5
$Ru3d_{5/2(sat)}$	281.05	1.57	1,246	1.7
$Ru3d_{3/2(sat)}$	285.22	1.68	860	1.2
C-C, C-H	285.01	1.34	3,178	53.8
C-OH	285.44	1.81	1,599	27.1
C=O	286.08	1.73	602	10.2

Name	Position	FWHM	Raw Area	%At Conc
$Ru3d_{5/2}$	280.45	0.64	1,678	3.0
$Ru3d_{3/2}$	284.62	0.95	1,158	2.1
$Ru3d_{5/2(sat)}$	281.1	1.22	625	1.1
$Ru3d_{3/2(sat)}$	285.27	1.82	431	0.8
C-C, C-H	285.15	1.33	2,149	48.5
C-OH	285.42	1.65	1,525	34.4
C=O	286.26	1.8	447	10.1

RuBZY20

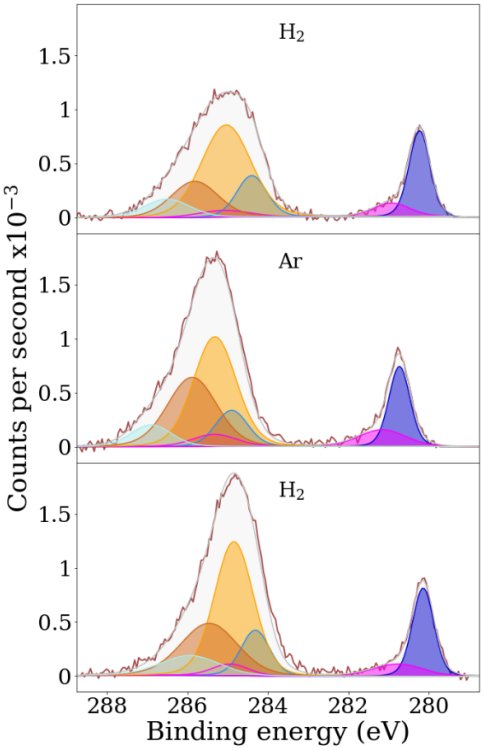

Name	Position	FWHM	Raw Area	%At Conc
$Ru3d_{5/2}$	280.23	0.62	543	2.0
$Ru3d_{3/2}$	284.4	0.88	375	1.3
$Ru3d_{5/2(sat)}$	280.93	1.07	150	0.5
$Ru3d_{3/2(sat)}$	285.1	1.48	104	0.4
C-C, C-H	285.04	1.45	1,370	61.4
C-OH	285.82	1.37	509	22.8
C=O	286.51	1.35	257	11.5

Name	Position	FWHM	Raw Area	%At Conc
$Ru3d_{5/2}$	280.73	0.62	509	1.4
$Ru3d_{3/2}$	284.9	0.95	351	1.0
$Ru3d_{5/2(sat)}$	281.16	1.36	234	0.7
$Ru3d_{3/2(sat)}$	285.33	1.29	161	0.5
C-C, C-H	285.32	1.26	1,417	50.4
C-OH	285.89	1.45	1,031	36.6
C=O	286.91	1.19	266	9.5

Name	Position	FWHM	Raw Area	%At Conc
$Ru3d_{5/2}$	280.14	0.63	573	1.6
$Ru3d_{3/2}$	284.31	0.84	395	1.1
$Ru3d_{5/2(sat)}$	280.77	1.46	185	0.5
$Ru3d_{3/2(sat)}$	284.94	1.06	128	0.4
C-C, C-H	284.85	1.14	1,575	54.0
C-OH	285.46	1.66	888	30.5
C=O	285.94	1.72	349	12.0

RuBZ

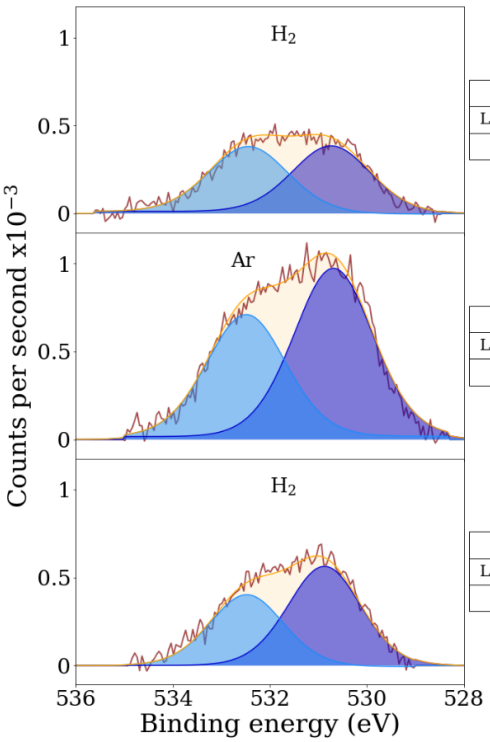

Name	Position	FWHM	Raw Area	%At Conc
Lattice oxide	530.73	1.92	799	50.7
Hydroxides	532.44	1.92	776	49.3

Name	Position	FWHM	Raw Area	%At Conc
Lattice oxide	530.69	1.93	1,994	58.0
Hydroxides	532.49	1.93	1,447	42.0

Name	Position	FWHM	Raw Area	%At Conc
Lattice oxide	530.87	1.78	1,095	58.5
Hydroxides	532.47	1.78	777	41.5

RuBZY10

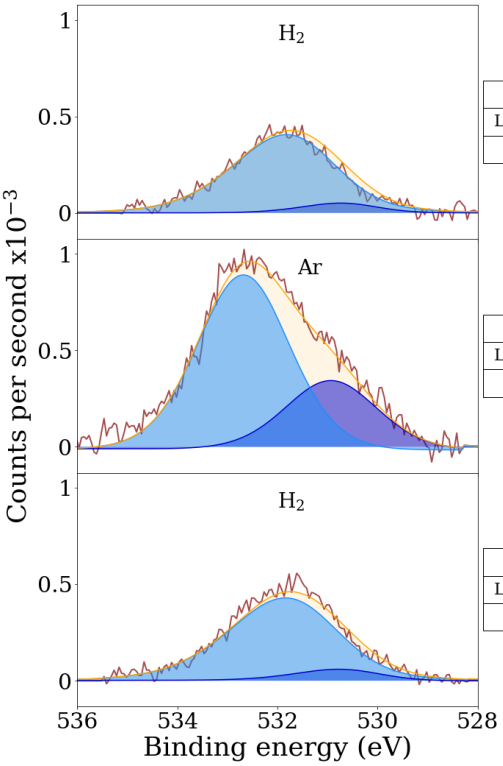

Name	Position	FWHM	Raw Area	%At Conc
Lattice oxide	530.5	1.7	105	8.6
Hydroxides	531.5	2.31	1,120	91.4

Name	Position	FWHM	Raw Area	%At Conc
Lattice oxide	530.93	2.16	838	28.4
Hydroxides	532.68	2.16	2,112	71.6

Name	Position	FWHM	Raw Area	%At Conc
Lattice oxide	530.5	1.94	142	10.2
Hydroxides	531.5	2.44	1,250	89.8

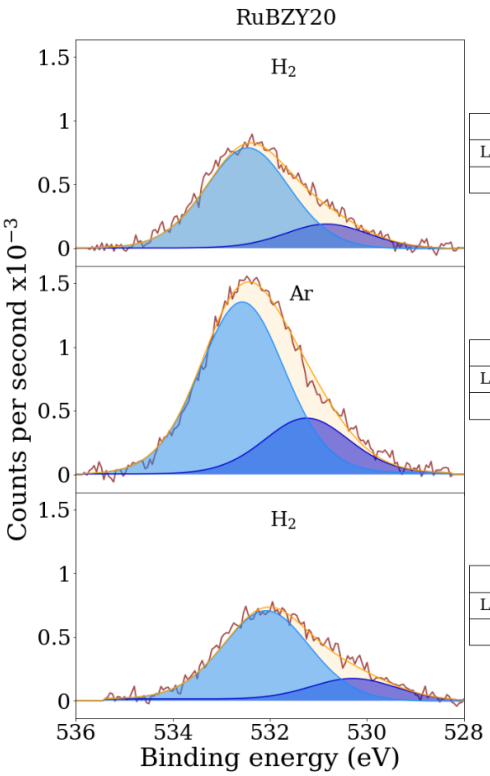

Name	Position	FWHM	Raw Area	%At Conc
Lattice oxide	530.83	2.04	428	19.7
Hydroxides	532.46	2.04	1,746	80.3

Name	Position	FWHM	Raw Area	%At Conc
Lattice oxide	531.24	2.07	968	24.3
Hydroxides	532.57	2.07	3,017	75.7

Name	Position	FWHM	Raw Area	%At Conc
Lattice oxide	530.28	2.11	406	20.2
Hydroxides	532.07	2.11	1,604	79.8

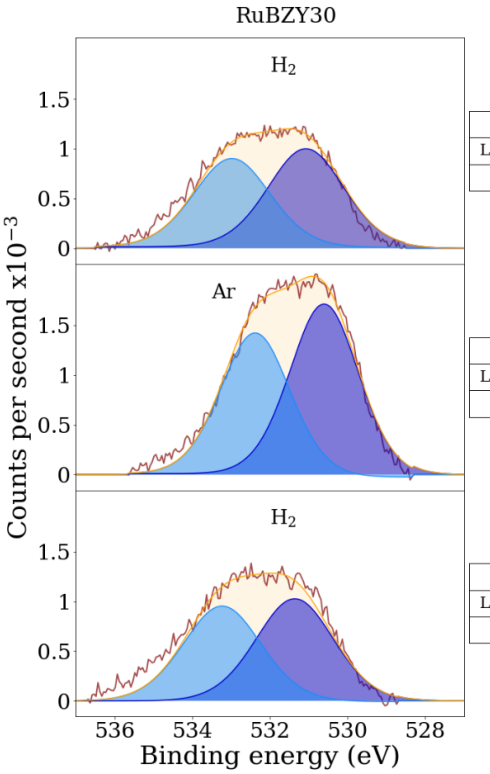

Name	Position	FWHM	Raw Area	%At Conc
Lattice oxide	531.07	2.31	2,480	52.7
Hydroxides	532.98	2.31	2,228	47.3

Name	Position	FWHM	Raw Area	%At Conc
Lattice oxide	530.6	2.09	3,921	54.9
Hydroxides	532.38	2.09	3,224	45.1

Name	Position	FWHM	Raw Area	%At Conc
Lattice oxide	531.36	2.37	2,647	51.9
Hydroxides	533.23	2.37	2,450	48.1

Figure S10. Near-ambient pressure XPS of RuBZY, RuBZY10, RuBZY20, and RuBZY30.

Sample	Element	Composition (total) / %wt	Composition (support) / %wt	Calculated B-site occupancy / %
RuBZ (pre)	Ru	6.569	N/A	
	Y	0.005	0.005	
RuBZY20 (pre)	Ru	8.203	N/A	
	Y	5.732	6.244	19.39
RuBZY20 (post)	Ru	9.974	N/A	
	Y	5.896	6.549	20.06

Table S2. Catalyst composition from ICP-OES analysis (Optima 8300DV).

	Treatment	**Non-deuterated**		**Deuterated**			
	Refinement model			**No deuterium**		**Deuterium**	
Phase	**Material**	**BZY20**	**RuBZY20**	**D-BZY20**	**D-RuBZY20**	**D-BZY20**	**D-RuBZY20**
	No. bkg. parameters	24					
BZY support	R_{exp} / %	0.5782	0.6366	0.7018	0.6135	0.7015	0.6134
	R_{wp} / %	3.8735	2.8981	4.6343	3.3552	4.5542	3.3078
	R_p / %	2.5376	2.1157	3.1432	2.4649	3.1944	2.3635
	GoF	6.6992	4.5526	6.6039	5.4685	6.4918	5.3930
	Space group	*Pm-3m*					
	Lattice parameter						
	a / Å	4.22585(7)	4.2229(1)	4.2340(1)	4.2304(1)	4.2341(1)	4.2304(1)
	Volume / Å^3	75.464(4)	75.307(6)	75.903(5)	75.710(7)	75.905(5)	75.709(6)
	Phase density / g cm^{-3}	5.93(4)	6.0878(5)	5.92(5)	6.0554(5)	5.81(4)	6.059(1)
	Atomic positions						
	A site (Ba^{2+})	(0, 0, 0)					
	B site (Zr^{4+}/Y^{3+})	(0.5, 0.5, 0.5)					
	O^{2-} site	(0.0, 0.5, 0.5)					
	D^+ site	N/A		N/A		(0, 0, 0.5)	
	Occupancy						
	Ba^{2+}	1.00(1)		1.00(1)		0.98(1)	
	Zr^{4+}	0.790(6)		0.775(6)		0.778(6)	
	Y^{3+}	0.190(5)		0.176(6)		0.151(6)	
	O^{2-}	0.90(1)		1.00(1)		0.97(1)	
	D^+	N/A		N/A		0.037(13)	0.048(16)
	beq (= 8 $\pi^2 \times U_{iso}$) / Å^2						
	A site (Ba^{2+})	1.01(6)		0.80(7)		0.87(8)	
	B site (Zr^{4+}/Y^{3+})	1.48(7)		1.14(9)		1.2(1)	
	O^{2-} site	1.83(5)		2.23(6)		2.27(8)	
	D^+ site	N/A		N/A		20(7)	
Ruthenium metal	Space group	N/A	*P6$_3$/mmc*	N/A	*P6$_3$/mmc*	N/A	*P6$_3$/mmc*
	Lattice parameter						
	a / Å	N/A	2.697(2)	N/A	2.695(2)	N/A	2.694(2)
	c / Å	N/A	4.289(8)	N/A	4.307(8)	N/A	4.310(7)
	Volume / Å^3	N/A	27.03(6)	N/A	27.09(6)	N/A	27.09(5)
	Phase density / g cm^{-3}	N/A	37.26(8)	N/A	37.18(8)	N/A	37.17(7)
	Composition/ %wt.	N/A	1.20(8)	N/A	1.53(9)	N/A	1.51(8)
	Ru atomic position	N/A	(1/3, 2/3, 0.25)	N/A	(1/3, 2/3, 0.25)	N/A	(1/3, 2/3, 0.25)
	Ru occupancy	N/A	1 *	N/A	1 *	N/A	1 *
	Ru *beq* / Å^2	N/A	1 *	N/A	1 *	N/A	1 *

Table S3. Details for the Rietveld refinement of deuterated BZY20 and deuterated RuBZY20, with and without an interstitial deuterium site. Parameters fixed at unity denoted by *.

Mechanistic considerations

We have previously studied the rate equation for ammonia synthesis by examining the reaction orders of N_2 over Ru on different supports, which show almost the same positive order (around 1 to 1.5) in the rate equation for ammonia synthesis over ruthenium catalysts as similar to typical literature value.[10] The value indicates the dynamic adsorption of N_2 is critically important in the rate-determining step (dissociative adsorption mechanism). It was found that the reaction order of H_2 can be greatly altered from typical negative or zero order (H_2 poisoned Ru) on inert supports to positive order (rate dependent on H_2) if some hydrogen-trapped supports are used.

In this paper, we have focussed on the correlation of the rate for ammonia production with the proton concentration (proton trap site) on the BYZ support with the H_2 reaction order. First, we consider a Ru metal surface that could be under dynamic equilibrium with gaseous H_2 (classical Langmuir–Hinshelwood) and the surface hydrogen traps on the support if slow may not be able to alter such process under steady-state conditions. On the other hand, the kinetics for hydrogen adsorption on metal can still be altered provided that there is a faster but reversible hydrogen traps/storage on the support. Kitano et al. have recently studied the kinetics of nitrogen and hydrogen isotope exchange and hydrogen adsorption/desorption reactions over Ru/C12A7:e^-.[15] They concluded that the rate-determining step of ammonia synthesis involves rapid but reversible storage and release of hydrogen atoms on the Ru/C12A7:e^- surface on the basis of observed hydrogen absorption/desorption kinetics.

In addition, as shown from the Fig. 5, we doped Y into BZ which would increase the concentration of oxygen vacancies. However, we did not see the progressive linear relationship of rate versus doping (oxygen vacancies) concentration but was found to be optimum at 20% Y, afterwards declining. There appears to be no simple direct relationship between the oxygen vacancies of the support and the weakening of hydrogen adsorption on Ru. We also observed the effect of hydrogen trapping near Y by our neutron work. As a result, we adopted a similar view as Kitano et al., that the surface traps on the support can affect the adsorption kinetics of the overlying Ru. However, further proof is required in future through the careful

study of adsorption heat and saturation coverage of hydrogen, and temperature-programmed desorption measurements.

Notice that there appears to be no initial rate or directional limitations as anticipated for homogeneous Ru sites on a single crystalline support surface. However, for polycrystalline powder catalysts with randomly distributed ruthenium, there are facets of the Ru metal crystallites and BYZ support that show different relative adsorption for H_2 and N_2. For example, hydrogen poisoning for more active Ru facets can be alleviated by conducting the H_2 species to other facets with weaker adsorption for reversible H_2 desorption via the support and its local proton conductivity. The H_2 reservoir and the fast reversible H_2 storage and dissociation from the BYZ perovskite will then help the overall H_2 poisoning over the overlying Ru under dynamic conditions. In these catalytic investigations we particularly used continuous flow reactors, the dynamic equilibrium in which strong Ru active sites are made available to dinitrogen adsorption more often than without the proton reservoir can be obtained.

References

(1) Han, D.; Shinoda, K.; Sato, S.; Majima, M.; Uda, T. Correlation between Electroconductive and Structural Properties of Proton Conductive Acceptor-Doped Barium Zirconate. *J. Mater. Chem. A* **2014**, *3* (3), 1243–1250. https://doi.org/10.1039/C4TA05701E.

(2) Kitano, M.; Inoue, Y.; Sasase, M.; Kishida, K.; Kobayashi, Y.; Nishiyama, K.; Tada, T.; Kawamura, S.; Yokoyama, T.; Hara, M.; Hosono, H. Self-Organized Ruthenium–Barium Core–Shell Nanoparticles on a Mesoporous Calcium Amide Matrix for Efficient Low-Temperature Ammonia Synthesis. *Angew. Chem.* **2018**, *130* (10), 2678–2682. https://doi.org/10.1002/ange.201712398.

(3) Kitano, M.; Inoue, Y.; Yamazaki, Y.; Hayashi, F.; Kanbara, S.; Matsuishi, S.; Yokoyama, T.; Kim, S.-W.; Hara, M.; Hosono, H. Ammonia Synthesis Using a Stable Electride as an Electron Donor and Reversible Hydrogen Store. *Nat Chem* **2012**, *4* (11), 934–940. https://doi.org/10.1038/nchem.1476.

(4) Wang, Z.; Liu, B.; Lin, J. Highly Effective Perovskite-Type BaZrO3 Supported Ru Catalyst for Ammonia Synthesis. *Applied Catalysis A: General* **2013**, *458*, 130–136. https://doi.org/10.1016/j.apcata.2013.03.037.

(5) Sato, K.; Imamura, K.; Kawano, Y.; Miyahara, S.; Yamamoto, T.; Matsumura, S.; Nagaoka, K. A Low-Crystalline Ruthenium Nano-Layer Supported on Praseodymium Oxide as an Active Catalyst for Ammonia Synthesis. *Chem. Sci.* **2016**, *8* (1), 674–679. https://doi.org/10.1039/C6SC02382G.

(6) Shimoda, N.; Kimura, Y.; Kobayashi, Y.; Kubota, J.; Satokawa, S. Ammonia Synthesis over Yttrium-Doped Barium Zirconate and Cerate-Based Perovskite-Type Oxide Supported Ruthenium Catalysts. *International Journal of Hydrogen Energy* **2017**, *42* (50), 29745–29755. https://doi.org/10.1016/j.ijhydene.2017.10.108.

(7) Wang, P.; Chang, F.; Gao, W.; Guo, J.; Wu, G.; He, T.; Chen, P. Breaking Scaling Relations to Achieve Low-Temperature Ammonia Synthesis through LiH-Mediated Nitrogen Transfer and Hydrogenation. *Nature Chemistry* **2017**, *9* (1), 64–70. https://doi.org/10.1038/nchem.2595.

(8) Ogura, Y.; Sato, K.; Miyahara, S.; Kawano, Y.; Toriyama, T.; Yamamoto, T.; Matsumura, S.; Hosokawa, S.; Nagaoka, K. Efficient Ammonia Synthesis over a Ru/La 0.5 Ce 0.5 O 1.75 Catalyst Pre-Reduced at High Temperature. *Chemical Science* **2018**, *9* (8), 2230–2237. https://doi.org/10.1039/C7SC05343F.

(9) Lin, B.; Liu, Y.; Heng, L.; Wang, X.; Ni, J.; Lin, J.; Jiang, L. Morphology Effect of Ceria on the Catalytic Performances of Ru/CeO2 Catalysts for Ammonia Synthesis. *Ind. Eng. Chem. Res.* **2018**, *57* (28), 9127–9135. https://doi.org/10.1021/acs.iecr.8b02126.

(10) Wu, S.; Peng, Y.-K.; Chen, T.-Y.; Mo, J.; Large, A.; McPherson, I.; Chou, H.-L.; Wilkinson, I.; Venturini, F.; Grinter, D.; Ferrer Escorihuela, P.; Held, G.; Tsang, S. C. E. Removal of Hydrogen Poisoning by Electrostatically Polar MgO Support for Low-Pressure NH3 Synthesis at a High Rate over the Ru Catalyst. *ACS Catal.* **2020**, *10* (10), 5614–5622. https://doi.org/10.1021/acscatal.0c00954.

(11) Ozaki, A.; Taylor, H.; Boudart, M. Kinetics and Mechanism of the Ammonia Synthesis. *Proceedings of the Royal Society of London Series A* **1960**, *258*, 47–62. https://doi.org/10.1098/rspa.1960.0174.

(12) Rosowski, F.; Hornung, A.; Hinrichsen, O.; Herein, D.; Muhler, M.; Ertl, G. Ruthenium Catalysts for Ammonia Synthesis at High Pressures: Preparation, Characterization, and Power-Law Kinetics. *Applied Catalysis A: General* **1997**, *151* (2), 443–460. https://doi.org/10.1016/S0926-860X(96)00304-3.

(13) Shimizu, H.; Christmann, K.; Ertl, G. Model Studies on Bimetallic Cu/Ru Catalysts: II. Adsorption of Hydrogen. *Journal of Catalysis* **1980**, *61* (2), 412–429. https://doi.org/10.1016/0021-9517(80)90388-7.

(14) Shetty, S.; Jansen, A. P. J.; van Santen, R. A. Active Sites for N2 Dissociation on Ruthenium. *J. Phys. Chem. C* **2008**, *112* (46), 17768–17771. https://doi.org/10.1021/jp8085478.

(15) Kitano, M.; Kanbara, S.; Inoue, Y.; Kuganathan, N.; Sushko, P. V.; Yokoyama, T.; Hara, M.; Hosono, H. Electride Support Boosts Nitrogen Dissociation over Ruthenium Catalyst and Shifts the Bottleneck in Ammonia Synthesis. *Nat Commun* **2015**, *6* (1), 6731. https://doi.org/10.1038/ncomms7731.